IOP Publishing Phys. Med. Biol. 63 (2018) 155019 (18pp) https://doi.org/10.1088/1361-6560/aacddf

Physics in Medicine & Biology

IPEM Institute of Physics and Engineering in Medicine

CrossMark

RECEIVED
2 February 2018

REVISED
15 June 2018

ACCEPTED FOR PUBLICATION
20 June 2018

PUBLISHED
31 July 2018

PAPER

Vesselness-constrained robust PCA for vessel enhancement in x-ray coronary angiograms

Jingyang Zhang[1], **Guotai Wang**[2], **Hongzhi Xie**[3,4], **Shuyang Zhang**[3], **Zhenghui Shi**[1] **and Lixu Gu**[1,4]

[1] School of Biomedical Engineering, Shanghai Jiao Tong University, Shanghai, People's Republic of China
[2] Translational Imaging Group, Centre for Medical Image Computing, University College London, London, United Kingdom
[3] Department of Cardiothoracic Surgery, Peking Union Medical College Hospital, Beijing, People's Republic of China
[4] Authors to whom any correspondence should be addressed.

E-mail: gulixu@sjtu.edu.cn (L Gu) and xiehongzhi@medmail.com.cn (H Xie)

Keywords: robust principal component analysis, layer separation, vessel-like appearance prior, vessel motion, x-ray coronary angiogram

Abstract

Effective vessel enhancement in x-ray coronary angiograms (XCA) is essential for the diagnosis of coronary artery disease, yet challenged by complex background structures of varying intensities as well as motion patterns. As a typical layer-separation method, robust principal component analysis (RPCA) has been proposed to automatically improve vessel visibility via sparse and low-rank decomposition. However, the attenuated motion of vessels in x-ray angiograms leads to the unsatisfactory vessel enhancement performance of the decomposition framework.

To address this problem, we propose a vesselness-constrained RPCA method (VC-RPCA), where a vessel-like appearance prior is incorporated into the layer separation framework for accurate vessel enhancement. We first pre-compute the vessel-like appearance prior based on a Frangi filter to highlight the curvilinear structures. After removing large-scale background structures via a morphological closing operation, we then integrate the pre-computed vessel-like appearance prior into a low-rank decomposition framework to separate the fine vessel structures. In addition, we develop an adaptive regularization strategy that imposes structured-sparse constraints to solve the scale issue and capture vessels without salient motion.

The proposed method was validated on 13 clinical XCA sequences containing 777 images in total. The contrast-to-noise ratio, Dice coefficient and area under the ROC curve were employed for quantitative evaluation of the vessel enhancement performance. Experiments show that (1) the adaptive regularization strategy helps to obtain a complete coronary tree in the separated vessel layer; (2) our low-rank decomposition framework is robust against false positive/negative responses of the Frangi filter; and (3) the proposed VC-RPCA is computationally fast and outperforms other state-of-the-art RPCA methods for vessel enhancement in the full-contrast and low-contrast scenarios. The results demonstrate that the proposed VC-RPCA can accurately separate coronary arteries and prominently improve vessel visibility in x-ray angiograms.

1. Introduction

1.1. Background

Coronary artery disease is the major cause of death globally (Wang *et al* 2016), killing 8.9 million people and affecting over 110 million people worldwide in 2015 (Vos *et al* 2016). The development of medical imaging such as x-ray angiography (XA), computed tomography angiography (CTA) and magnetic resonance angiography (MRA) makes it possible to diagnose this disease at an early time. Among these methods, the x-ray coronary angiogram (XCA) is regarded as the gold standard for diagnosis and pre-intervention decision-making in coronary artery disease. This imaging modality is based on the radiographic visualization of coronary arteries with the injection of a radiopaque contrast agent. The complex 3D structure of contrast-filled vessels is projected and visualized on a 2D x-ray angiogram plane. Figure 1 shows the procedure of a coronary angiography, where an XCA sequence records the distribution variation of a contrast agent flowing through the vessel network over

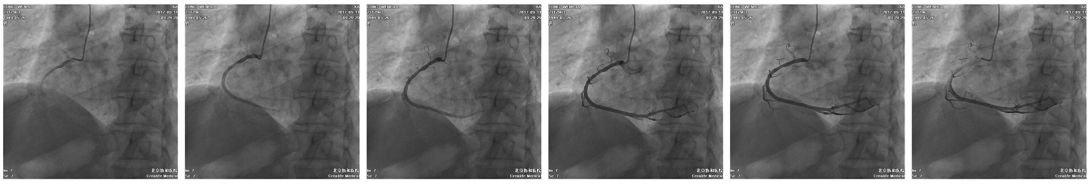

Figure 1. An example of an XCA sequence: (a) at the 12th frame; (b) at the 18th frame; (c) at the 22th frame; (d) at the 35th frame; (e) at the 47th frame; (f) at the 58th frame.

a number of frames. At the beginning, a catheter is inserted into the target vessel and the radiopaque contrast agent is injected through it. The contrast agent then gradually fills and visualizes the entire vessel lumen. Finally, it is washed out by flowing blood. In addition to the static appearance cue contained in a single frame, an XCA sequence can also provide a beneficial motion cue during the coronary angiography. Therefore, XCA sequences are widely used in clinical workflow.

In XCA, several factors lead to poor vessel visibility. First, the angiograms are blurred by overlapping opaque and semi-transparent background structures with varying intensities and motion patterns. Second, due to the side effects of the x-ray contrast agent, such as allergic reaction and nephrotoxicity (Andreucci *et al* 2014), radiologists are encouraged to use a minimal concentration of contrast agent in clinical x-ray angiography. The low contrast concentration even causes poorer vessel visibility, leading to more difficulties for the accurate diagnosis of coronary artery disease. To address this problem, vessel enhancement is highly desired to improve vessel visibility in a complex background. It is also a prerequisite for further processing of the XCA, such as vessel segmentation (Lesage *et al* 2009), the reconstruction of 3D coronary arteries (Çimen *et al* 2016), statistical coronary motion analysis (Panayiotou *et al* 2014) and the registration of XCA and CTA (Baka *et al* 2013). Layer separation is one of the most effective methods to achieve vessel enhancement, in particular for coronary arteries (Fischer *et al* 2015). It assumes the XCA to be a superposition of various layers containing different structures, which have inherently different motion characteristics. By separating the vessels (the vessel layers) from the complex background, the layer separation method can improve vessel visibility in the XCA sequence.

1.2. Related works

There are two main types of existing layer separation method: those based on motion estimation and those based on blind source separation.

In motion-estimation-based layer separation methods, each separated layer is characterized by its inherent motion information. The reliable motion estimation of each layer between adjacent frames is essential, though it is challenged by varying respiratory and cardiac motion patterns as well as noise intensity variation in the background. These methods can also be considered as generalized digital subtraction angiography (DSA, Ungi *et al* 2009) with two or even more separated layers. For two-layer coronary DSA, Zhu *et al* (2009) integrated uncertainty propagation and dense motion estimation into a Bayesian framework to achieve layer separation. However, motion estimation for the two-layer separation method is difficult, due to the mixture of cardiac and respiratory motion in a single dynamic mask. This issue can be solved by multi-layer separation methods, where the inflexible motion estimation is divided into several independent estimations of different motion patterns. Therefore, multi-layer methods can exploit the discriminative motion characteristics inherent in different anatomical structures to achieve better layer separation. Zhang *et al* (2009) employed a multi-scale framework to optimize the multi-layer separation problem by minimizing a reconstruction error. It utilized thin plate spline interpolation to refine the complex motion field of vessels, which relied on manually selected control points at the finest scale. Towards a more robust layer separation framework, Fischer *et al* (2015) developed an anti-noise probabilistic model by introducing a robust penalty term and a bilateral total variation regularization term. This model can sufficiently suppress noise in the image formation model, and achieve satisfactory edge-preservation performance. In addition, Timinger *et al* (2005) and Baka *et al* (2015) improved motion-estimation-based layer separation methods by complementing cardiac motion with the surrogate-driven estimation of respiratory motion. Nevertheless, it is still hard to explicitly achieve accurate motion estimation, and is regarded as a typical chicken-and-egg problem for multi-layer separation in XCA.

Instead of relying on the ill-posed motion estimation, some other methods view the layer separation task as a classical blind source separation issue. Considering an angiogram sequence to be a mixture of two non-Gaussian independent signals, Tang *et al* (2012) applied independent component analysis (ICA, Hyvärinen and Oja 2000) to separate the angiogram into a background layer and a vessel layer. In addition to ICA, Candès *et al* (2011) proposed a principal component pursuit (PCP) method to solve the blind source separation issue in a sparse,

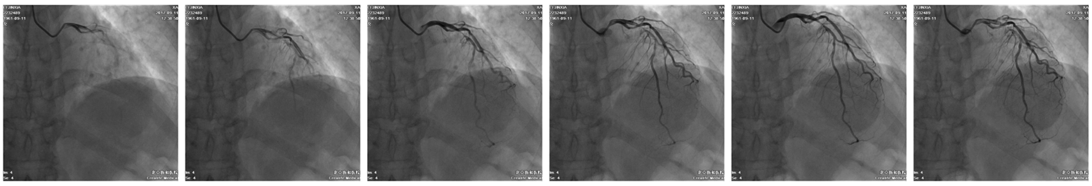

(a) (b) (c) (d) (e) (f)

Figure 2. An example for clarifying the origin of attenuate motion in an XCA sequence: (a)–(c) show the influence of the flowing contrast agent; (d)–(f) show the influence of the suboptimal angiographic viewing angle.

low-rank decomposition framework, which is referred to as robust principal component analysis (RPCA). This imposes a nuclear norm constraint on the background and implicitly models quasi-static motion as a low-rank matrix. Ma *et al* (2015) adopted this method to separate each XCA frame into a breathing layer, a quasi-static background layer and a vessel layer for percutaneous coronary intervention. Although the IALM-BLWS strategy (Lin and Wei 2010) and the FPCP method (Rodriguez and Wohlberg 2013) were developed to accelerate the low-rank decomposition process, these methods require all frames or a mini-batch of data (Volpi *et al* 2015) in the image sequence, and cannot meet real-time requirements in the clinical workflow. Ma *et al* (2017) extended the PCP method to an online version for computation and storage efficiency in a prospective setting. Other than the naïve-sparsity-constraint-based foreground prior used in the PCP optimization framework, Wang *et al* (2012) modeled foreground outliers as the Laplace error in a probabilistic robust matrix factorization framework (PRMF). Furthermore, the foreground prior can be promoted by imposing specific motion constraints (Gao *et al* 2014, Jin *et al* 2017) or additional smoothness constraints (Becker *et al* 2011, Zhou *et al* 2013) on candidate foreground objects. For motion constraint-based prior foregrounds, Gao *et al* (2014) designed a novel block-sparsity of moving foreground objects based on salient motion analysis. The heavily relied upon motion tracker hampers the effectiveness of this method due to noise intensity variation in the XCA. Instead of the explicit motion estimation of the moving foreground object, Jin *et al* (2017) proposed total variation regularization to guarantee implicit motion coherency (MRC-RPCA) for the extracted vessel trajectories. For smoothness-constraint-based prior foregrounds, Becker *et al* (2011) provided a unified template for sparse signal recovery with a flexible smoothness constraint (TFOCS). Zhou *et al* (2013) adopted an elaborate prior Markov random field (MRF) to strengthen the smoothness constraint on the contiguous outliers in a low-rank representation (DECOLOR).

Despite the various implementations of existing RPCA methods, they still present some limitations for the accurate separation of vessels in an XCA sequence.

First, the existing foreground priors used by low-rank decomposition are introduced to deal with general video surveillance (Bouwmans *et al* 2017), while lacking the characteristic customization for vessel separation in an XCA sequence. Unlike the foreground objects in video surveillance, which have a relatively regular motion pattern, some of the contrast-filled vessels visualized in angiogram sequences usually present non-salient motion for a period of time—so-called 'attenuate motion'. This attenuate motion can be caused by both the flowing contrast agent and the suboptimal angiographic viewing angle. On the one hand, the contrast agent flows at different velocities through different vessel branches, as shown in figures 2(a)–(c). It is flowing fast to the distal vessel in figures 2(a) and (b). Then in figure 2(c), the contrast agent fills the vessel network and its inflow motion can hardly be observed anymore. Therefore, the visualized vessels in figure 2(c) suffer from attenuate motion compared with figures 2(a) and (b). On the other hand, due to the foreshortening of 2D projections, a suboptimal angiographic viewing angle (Dumay *et al* 1994) reduces the 3D motions of the vessel itself and deteriorates the attenuate motion issue. This is demonstrated in figures 2(d)–(f), where the physically apparent motion of the main coronary artery (MCA) is buried in the 2D projection planes at the given angiographic viewing angle. This visualized MCA remains almost static during the long angiography period from the 30th to the 44th frame. The existing foreground priors cannot provide a robust constraint on contrast-filled vessels without salient motion in the angiogram sequence. Therefore, the low-rank decomposition in the existing RPCA methods cannot ensure accurate vessel enhancement as well as the simultaneously effective removal of background disturbance.

Second, classical RPCA methods use a globally-fixed regularization parameter, which cannot handle the perennial scale issue (Gao *et al* 2014) in background/foreground separation tasks. In XCA images, a single regularization parameter is not suitable for the detection of vessels of various sizes. Even worse, the attenuate vessel motion degrades the decomposition process, creating more challenges for vessel separation with a globally-fixed regularization parameter.

Third, a potential application of layer separation is to improve vessel visibility under the condition of low-contrast concentration. However, except for PCP, none of these RPCA methods have been investigated in the low-contrast scenario.

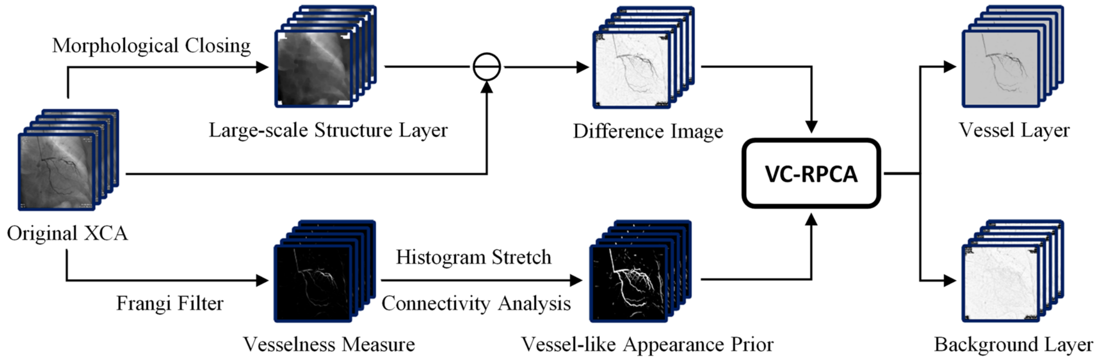

Figure 3. The framework of our proposed VC-RPCA method.

1.3. Contribution

We propose a vesselness-constrained robust principal component analysis (VC-RPCA) with a novel vessel-like appearance prior that is robust enough to attenuate vessel motion in XCA sequences. Considering the curvilinear nature of vessels, the proposed foreground prior is pre-computed based on a Frangi filter to capture the curvilinear structures, which have a so-called 'vessel-like' appearance. We first use a morphological closing operation to remove large-scale background structures, and then integrate the pre-computed vessel-like appearance prior into a low-rank decomposition framework to further accurately separate coronary arteries. Our contribution is four-fold:

(a) To the best of our knowledge, we are the first to integrate a vessel-like appearance prior into a low-rank decomposition framework for vessel enhancement in XCA.
(b) We propose an adaptive regularization strategy that contributes to sufficient vessel extraction, despite the attenuate vessel motion in angiogram sequences.
(c) We adopt low-rank decomposition to relieve the notorious false positive and false negative issues of the Frangi filter.
(d) We validate the proposed method under conditions of low-contrast concentration, which has rarely been investigated by state-of-the-art RPCA methods.

2. Method

The proposed VC-RPCA method models an XCA as a superposition of three different layers: a large-scale structure layer containing a diaphragm border and a pericardium contour, a background layer containing the sternum, ribs and vertebral bodies, and a vessel layer containing coronary arteries. As shown in figure 3, our VC-RPCA method consists of three main parts: (1) removal of the large-scale structure layer from the original XCA; (2) generation of the vessel-like appearance prior based on the Frangi filter; and (3) separation of the vessel layer from the background layer via the proposed VC-RPCA decomposition.

2.1. Removal of large-scale background structures

To prevent artifacts being left in the vessel layer due to respiratory and cardiac motion, and to avoid the false positives of the vessel-like appearance prior due to the confusing curvilinear appearance, the layer that contains large-scale background structures, such as the diaphragm and pericardium, is extracted and removed before VC-RPCA decomposition.

To obtain a large-scale structure layer, we adopt a morphological closing operation with a structural disk element to remove thin structures from the original XCA. The size of the structural element is determined by the maximal coronary diameter, so that the diaphragm border and pericardium contour can be included in the large-scale structure layer. We subtract the obtained large-scale structure layer from the original XCA to get a difference image containing target coronary vessels. The difference image is then separated into a vessel layer and a background layer by the proposed VC-RPCA decomposition framework, which is described in section 2.3.

2.2. Generation of vessel-like appearance prior

The curvilinear feature, which is one of the most intuitive features of vessels, is referred to as a vessel-like appearance in this paper, and is evaluated by the vesselness measure at pixel level. To ensure a sufficient vesselness measure for the entire coronary tree, the proposed appearance prior is improved by a simple spatial coherency constraint.

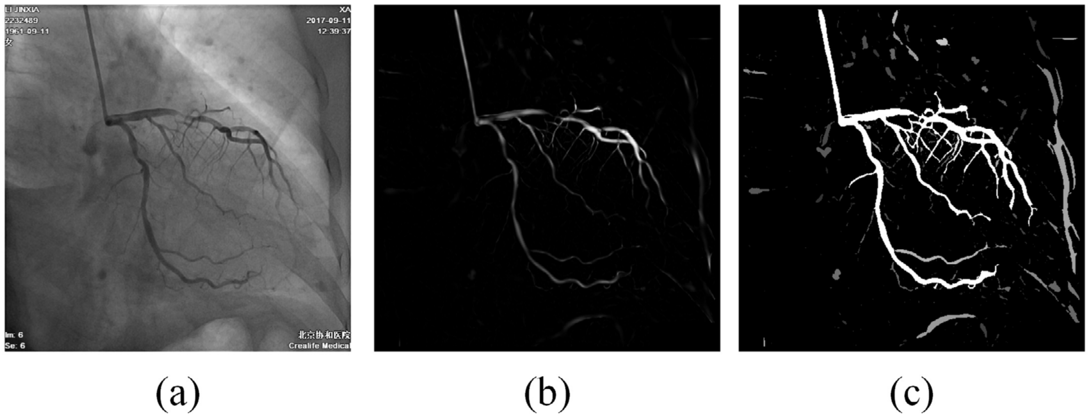

Figure 4. The generation of the vessel-like appearance prior: (a) the original XCA; (b) the vesselness measure obtained by the Frangi filter; (c) the vessel-like appearance prior after histogram stretch and connectivity analysis.

In the first step of generating the vessel-like appearance prior, we utilize a Frangi filter (Frangi *et al* 1998), a classical tubular detector, to obtain the original vesselness measure at each pixel in the XCA. The curvature values in different directions provide effective information for the detection of curvilinear structures. The curvature at each pixel is a second order property and can be captured by the eigensystem of the Hessian matrix. The two eigenvalues λ_1 and λ_2 ($\lambda_1 < \lambda_2$) of the Hessian matrix reflect the curvature along and perpendicular to the curvilinear structure direction, respectively. The vesselness measure $V(i,s)$, which combines the eigenvalues of each pixel i at scale s, is defined as:

$$V(i,s) = \begin{cases} 0, & \text{if } \lambda_2(i,s) > 0 \\ \exp\left(-\frac{R_B^2(i,s)}{2b^2}\right)\left(1-\exp\left(-\frac{S^2(i,s)}{2c^2}\right)\right) & \text{otherwise} \end{cases}, \tag{1}$$

where the blobness measure $R_B(i,s) = |\lambda_1(i,s)| / |\lambda_2(i,s)|$ represents the eccentricity of the second order ellipse, and the second order structureness $S(i,s) = \sqrt{\sum_{j=1,2} \lambda_j^2(i,s)}$ accounts for the Frobenius norm of the Hessian matrix. The sensitivity of $R_B(i,s)$ and $S(i,s)$ is controlled by parameters b and c respectively. The optimal vesselness measure $V(i)$ of the Frangi filter can be obtained by searching for the maximal value at different scales:

$$V(i) = \max_{s_{\min} \leqslant s \leqslant s_{\max}} V(i,s). \tag{2}$$

For the main vessels, the magnitude of $V(i)$ is high, i.e. a strong vesselness measure. However, for vessel branches, the magnitude of $V(i)$ is low, i.e. a weak vesselness measure, as shown in figure 4(b). Therefore, we adopt a vesselness histogram stretch to improve the vesselness measure for vessel-like structures, and then employ connectivity analysis to guarantee a simple spatial coherency for the vessel-like appearance prior. The histogram stretch is performed on the original vesselness measure for relatively effective thin branch detection and background suppression. The stretched range is parameterized by $[\theta_L, \theta_U]$ where θ_L is a lower bound and θ_U is an upper bound of vesselness measure. The stretched vesselness measure $\mathrm{SV}(i)$ of pixel i is defined as:

$$\mathrm{SV}(i) = \begin{cases} 0 & V(i) \leqslant \theta_L \\ \frac{1}{\theta_U - \theta_L}(V(i) - \theta_L) & \theta_L < V(i) \leqslant \theta_U \\ 1 & V(i) > \theta_U \end{cases}. \tag{3}$$

Then, connectivity analysis is utilized to detect all the connected regions of the stretched vesselness measure. The connected region of pixel i is denoted as $\mathrm{CR}(i)$. The vessel-like appearance prior $\mathrm{VAP}_{CR(i)}(i)$ of pixel i is computed as the averaged $\mathrm{SV}(j)$ in $\mathrm{CR}(i)$:

$$\mathrm{VAP}_{CR(i)}(i) = \frac{1}{N(\mathrm{CR}(i))} \sum_{j \in CR(i)} \mathrm{SV}(j), \tag{4}$$

where $N(\mathrm{CR}(i))$ is the number of pixels in $\mathrm{CR}(i)$. In general, the vessel-like appearance prior includes the improved vesselness measure $\mathrm{VAP}(i)$ and the location of the connected region $\mathrm{CR}(i)$, customized for the curvilinear feature of coronary arteries. Figure 4(c) shows the vessel-like appearance prior obtained for an example XCA frame. It is then integrated into the VC-RPCA low-rank decomposition framework, imposing a structured-sparse constraint on the vessels.

2.3. Vesselness-constrained RPCA

After subtracting the large-scale structure layer from the original XCA, the obtained difference image needs to be further separated into two layers: a background layer containing structures with a quasi-static motion, and a vessel layer containing contrast-filled vessels. In this subsection, the layer separation task is formulated as a VC-RPCA decomposition problem, which takes advantage of the vessel-like appearance prior and can be effectively solved by the inexact augmented Lagrange multiplier method.

2.3.1. Formulation of VC-RPCA

Given the difference image sequence obtained from section 2.1, we form a matrix $\boldsymbol{D} = (d_1, d_2, \ldots, d_t, \ldots, d_T)$, where d_t is a normalized difference image frame at the time point t. This matrix $\boldsymbol{D} \in \boldsymbol{R}^{m \times T}$ includes T frames, and each frame contains m pixels. From the perspective of matrix decomposition, $\boldsymbol{D}$ can be approximated as the sum of a low-rank matrix $\boldsymbol{L} \in \boldsymbol{R}^{m \times T}$ and a sparse matrix $\boldsymbol{S} \in \boldsymbol{R}^{m \times T}$. Due to the quasi-static motion pattern among these total T frames, background variation can be modeled by a low-rank matrix $\boldsymbol{L} = (l_1, l_2, \ldots, l_t, \ldots, l_T)$ with the nuclear norm constraint $\|\boldsymbol{L}\|_*$. To capture a foreground with a specific appearance prior, a structured-sparse matrix $\boldsymbol{S} = (S_1, S_2, \ldots, S_t, \ldots, S_T)$ is used to characterize the vessels, as they occupy only a small set of pixels in each frame. Therefore, our proposed VC-RPCA decomposition is formulated to separate a difference image sequence $\boldsymbol{D}$ into $\boldsymbol{L}$, a background layer sequence with low-rank constraint, and $\boldsymbol{S}$, a vessel layer sequence with a structured-sparse constraint:

$$\min_{\boldsymbol{L},\boldsymbol{S}} \|\boldsymbol{L}\|_* + \sum_k \lambda_k \|\boldsymbol{S_k}\|_F \quad \text{s.t. } \boldsymbol{D} = \boldsymbol{L} + \boldsymbol{S}, \tag{5}$$

$$\lambda_k = \alpha N(k)\left(1 - \mathrm{VAP}_k\right) / \sqrt{\max\left(m, T\right)}, \tag{6}$$

where k represents the index of the connected region from the pre-computed vessel-like appearance prior. $N(k)$ is the number of pixels in the kth connected region. The nuclear norm $\|\boldsymbol{L}\|_*$ is the sum of singular values of $\boldsymbol{L}$. $\|\boldsymbol{S_k}\|_F$ denotes the Frobenius norm of $\boldsymbol{S_k}$, which is the kth connected region of $\boldsymbol{S}$. We would like to emphasize that λ_k is an adaptive regularization parameter controlling the number of outliers in $\boldsymbol{S_k}$. The elaborate structured-sparse term $\sum_k \lambda_k \|\boldsymbol{S_k}\|_F$ is considered as the generalized $L_{2,1}$ norm (Gao *et al* 2014) in the low-rank decomposition. This contributes to solving the scale issue, and flexibly adjusts the detection sensitivity to the candidate foreground in $\boldsymbol{S_k}$ according to λ_k. Therefore, we propose an adaptive regularization strategy in equation (6), using a smaller λ_k with a larger vesselness VAP_k to better extract the vessel-like regions. Specifically, $N(k)$ is used to compensate the various scales of the Frobenius norm $\|\boldsymbol{S_k}\|_F$. The hyper-parameter α can be manually tuned to achieve the best possible layer separation performance in the vessel enhancement task. Regarded as a sparse error perturbing the low-rank pattern in $\boldsymbol{L}$ (Bouwmans *et al* 2017), the values of the vessel region in $\boldsymbol{S}$ tend to be negative in the decomposition framework, so that the contrast-filled vessels in $\boldsymbol{D}$ can be guaranteed to have a dark appearance.

2.3.2. Optimization

We adopt the inexact augmented Lagrange multiplier (inexact ALM) method (Lin *et al* 2010) to solve the convex optimization problem equation (4). This method has the advantage of demonstrating a five times faster convergence rate, higher precision and less memory consumption than the accelerated proximal gradient (APG) algorithm (Chen *et al* 2009). The augmented Lagrangian function is reformulated as:

$$f(\boldsymbol{L}, \boldsymbol{S}, \boldsymbol{Y}, \mu) = \|\boldsymbol{L}\|_* + \sum_k \lambda_k \|\boldsymbol{S_k}\|_F + \langle \boldsymbol{Y}, \boldsymbol{D} - \boldsymbol{L} - \boldsymbol{S} \rangle + \frac{\mu}{2}\|\boldsymbol{D} - \boldsymbol{L} - \boldsymbol{S}\|_F, \tag{7}$$

where $\boldsymbol{Y}$ is the Lagrange multiplier and μ is a positive scalar. We utilize an alternating direction method (ADM) to successively minimize $f(\boldsymbol{L}, \boldsymbol{S}, \boldsymbol{Y}, \mu)$ with respect to $\boldsymbol{L}$, $\boldsymbol{S}$, $\boldsymbol{Y}$ and μ, where each subproblem has been proven convex and can be solved by close-form solutions (Tang and Nehorai 2011). In subproblem A, $\boldsymbol{L}$ can be iteratively updated with the other variables fixed:

$$\boldsymbol{L} = \operatorname*{argmin}_{\boldsymbol{L}} f(\boldsymbol{L}, \boldsymbol{S}, \boldsymbol{Y}, \mu) = \operatorname*{argmin}_{\boldsymbol{L}} \frac{1}{\mu}\|\boldsymbol{L}\|_* + \frac{1}{2}\left\|\boldsymbol{L} - \left(\boldsymbol{D} - \boldsymbol{S} + \frac{\boldsymbol{Y}}{\mu}\right)\right\|_F^2 = \boldsymbol{U} S_{\mu^{-1}}[\boldsymbol{\Lambda}]\boldsymbol{V}^T, \tag{8}$$

where the matrices $\boldsymbol{U}$, $\boldsymbol{\Lambda}$ and $\boldsymbol{V}$ are obtained via the singular value decomposition (SVD) of $\boldsymbol{D} - \boldsymbol{S} + \mu^{-1}\boldsymbol{Y}$, and $S_{\mu^{-1}}[\boldsymbol{\Lambda}]$ denotes a singular value thresholding operator with a threshold μ^{-1}. The subproblem B optimizing $\boldsymbol{S}$ is:

$$\boldsymbol{S} = \operatorname*{argmin}_{\boldsymbol{S}} f(\boldsymbol{L}, \boldsymbol{S}, \boldsymbol{Y}, \mu) = \operatorname*{argmin}_{\boldsymbol{S}} \sum_k \frac{\lambda_k}{\mu}\|\boldsymbol{S_k}\|_F + \frac{1}{2}\left\|\boldsymbol{S_k} - \left(\boldsymbol{D_k} - \boldsymbol{L_k} + \frac{\boldsymbol{Y_k}}{\mu}\right)\right\|_F^2, \tag{9}$$

where $\boldsymbol{D_k}$, $\boldsymbol{L_k}$ and $\boldsymbol{Y_k}$ represent the kth connected region of $\boldsymbol{D}$, $\boldsymbol{L}$ and $\boldsymbol{Y}$, respectively. We achieve an optimal $\boldsymbol{S}$ by stacking all optimal $\boldsymbol{S_k}$, calculated by the block shrinkage operator $BS_{\mu^{-1}\lambda_k}[\boldsymbol{M_k}]$ (Tang and Nehorai 2011):

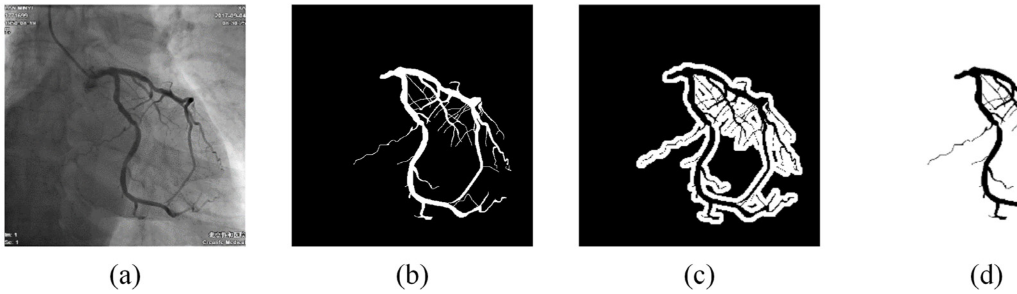

Figure 5. The definitions of foreground and different background masks for computing two versions of CNR: (a) the original XCA, (b) the foreground mask (white), (c) the local background mask (white), (d) the global background mask (white).

$$BS_{\mu^{-1}\lambda_k}\left[\boldsymbol{M_k}\right] = \begin{cases} \frac{\|\boldsymbol{M_k}\|_F - \mu^{-1}\lambda_k}{\|\boldsymbol{M_k}\|_F}\boldsymbol{M_k} & \text{if } \|\boldsymbol{M_k}\|_F > \mu^{-1}\lambda_k \\ 0 & \text{otherwise} \end{cases}, \tag{10}$$

Algorithm 1. Inexact ALM for VC-RPCA.

Input: Difference image sequence $\boldsymbol{D} \in \boldsymbol{R}^{m\times T}$, vessel-like appearance prior VAP;
Output: Background layer sequence $\boldsymbol{L} \in \boldsymbol{R}^{m\times T}$, vessel layer sequence $\boldsymbol{S} \in \boldsymbol{R}^{m\times T}$;
1. Initialization: $\boldsymbol{Y}^0 = \boldsymbol{D}/J(\boldsymbol{D}), \boldsymbol{S}^0 = \boldsymbol{0}, \mu^0 > 0, \rho > 1, k = 0$;
2. **while** not converged **do**
3. Subproblem A:
   solve $\boldsymbol{L}^{p+1} = \arg\min_{\boldsymbol{L}} f(\boldsymbol{L}, \boldsymbol{S}^p, \boldsymbol{Y}^p, \mu^p)$ via equation (8).
4. Subproblem B:
   compute the adaptive regularization parameter λ_k by equation (6).
   solve $\boldsymbol{S}^{p+1} = \arg\min_{\boldsymbol{S}} f\left(\boldsymbol{L}^{p+1}, \boldsymbol{S}, \boldsymbol{Y}^p, \mu^p\right)$ via equations (9) and (10).
5. $\boldsymbol{Y}^{p+1} = \boldsymbol{Y}^p + \mu^p\left(\boldsymbol{D} - \boldsymbol{L}^{p+1} - \boldsymbol{S}^{p+1}\right), \mu^{p+1} = \min\left(\rho\mu^p, 10^7\mu^0\right)$.
6. $p \leftarrow p + 1$.
7. **end while**
8. **return** $\boldsymbol{L}^p, \boldsymbol{S}^p$

where $\boldsymbol{M_k} = \boldsymbol{D_k} - \boldsymbol{L_k} + \mu^{-1}\boldsymbol{Y_k}$ is denoted for compact expression in the block shrinkage operator. We summarize the inexact ALM for the VC-RPCA in algorithm 1. The default setting of parameters is suggested by Lin *et al* (2010): $\mu^0 = 1.25/\|\boldsymbol{D}\|_2, \rho = 1.5$ and $J(\boldsymbol{D}) = \max\left(\|\boldsymbol{D}\|_2, \bar{\lambda}^{-1}\|\boldsymbol{D}\|_\infty\right)$, where $\|\cdot\|_2$ and $\|\cdot\|_\infty$ are the spectral norm and L_∞ norm, respectively.

3. Experiments and results

3.1. Data

We used 13 XCA sequences, including 777 frames in total, for the experiments. The data were acquired using a Philips UNIQ FD10 C-arm system with 15 frames s^{-1}. Each frame has 512×512 pixels. The frame number in a sequence ranges from 54 to 64. Every angiography sequence spans at least one whole cardiac cycle.

3.2. Quantitative evaluation criteria

Vessel visibility is regarded as the visual discrimination between vessels and other structures in angiograms. The contrast-to-noise ratio (CNR) can be used to quantitatively evaluate vessel visibility (Ma *et al* 2015, 2017, Jin *et al* 2017). It measures the contrast between the foreground and background pixel intensities in relation to the background standard deviation.

$$\text{CNR} = \frac{\left|\mu_f - \mu_b\right|}{\sigma_b}, \tag{11}$$

where μ_f and μ_b are the average pixel values of the foreground and background respectively. σ_b is the standard deviation of the background pixels and represents the residual background disturbance. A larger CNR reveals a higher vessel visibility for a vessel-enhanced result.

The CNR values were calculated with a foreground mask and a background mask. The foreground mask was determined by the manual segmented vessels from the original x-ray angiogram. We used a local background

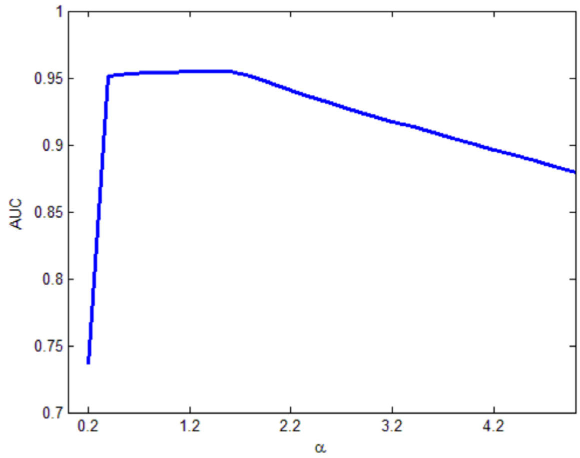

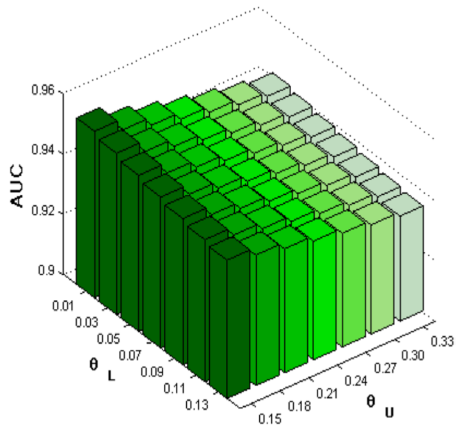

Figure 6. Systematic parameter analysis of the proposed VC-RPCA framework. (a) AUC as a function of the regularization-related parameter α. (b) The AUC as a function of the stretched lower bound θ_L and upper bound θ_U.

mask and a global background mask to calculate the local and global CNR respectively. The local background mask was defined as a 10 pixel-wide neighborhood around the foreground mask. The global background mask was defined as all regions outside the foreground mask. Figure 5 shows the definitions of the foreground and two versions of the background masks. For a given image, the CNR values for different algorithms were calculated with the same foreground and background masks.

To quantitatively assess the artifacts and the false positive/negative rate of enhancement, we further evaluated the performance with the Dice coefficient and the area under the receiver operating characteristics curve (AUC). Motivated by Merveille *et al* (2018), the Dice coefficient was calculated with the optimal global threshold:

$$\text{Dice} = \frac{2\text{TP}}{2\text{TP} + \text{FP} + \text{FN}}, \tag{12}$$

where TP stands for true positives and FP/FN stands for false positives/negatives. In addition, the AUC is the area under the ROC curve, and is related to the true positive and false positive rates (TPR, FPR). A higher Dice coefficient and AUC value indicate a better result, fewer artifacts and less error.

Similar to the evaluation for XCA sequences in Ma *et al* (2015, 2017) and Jin *et al* (2017), we randomly selected five frames from an angiogram sequence and used their average evaluation results as performance measurements for the sequence.

3.3. Experiment 1: parameter tuning and verification for VC-RPCA

The enhancement performance of the proposed VC-RPCA is affected by several parameters. We first adjusted these parameters to find their relatively optimal values, and then executed VC-RPCA with the optimal parameter setting in the following experiments.

To separate the large-scale structure layer, the size of the structural element used in the morphological operation was empirically chosen based on the physiological diameter of the coronary arteries. Considering the maximal diameter of 5–7 mm and a probable magnification of 1.5 (Dodge *et al* 1992, Perry *et al* 2013), we used a structural disk element 20 pixels in diameter (roughly larger than the vessel size) to remove thin curvilinear structures from the large-scale structure layer. In addition, the suggested parameters $b = 0.5$ and $c = 15$ for the Frangi filter were proven effective to roughly detect curvilinear structures in contrast x-ray angiograms (Frangi *et al* 1998). Therefore, we adopted this parameter setting to obtain the original vesselness measure, and then manually tuned the lower stretched bound θ_L, the upper stretched bound θ_U and the regularization-related parameter α. For each parameter, we traversed its value over a large range and found the optimal value that led to the best vessel enhancement performance quantified by AUC. Here, the AUC was employed as the metric instead of the CNR, since the CNR can easily be dominated by a very small standard deviation of the background region, as shown by Ma *et al* (2017). When tuning parameters use CNR as the objective for optimization, the optimal choice tends to yield an almost constant background region and ignore the details of the foreground region in the vessel layer, leading to an unrealistically high CNR value without enhancing some thin vessel branches. To avoid this problem, the objective for parameter optimization should consider the false negatives/positives of enhancement. Therefore, we employed AUC as a more reasonable objective to tune the parameters in the VC-RPCA.

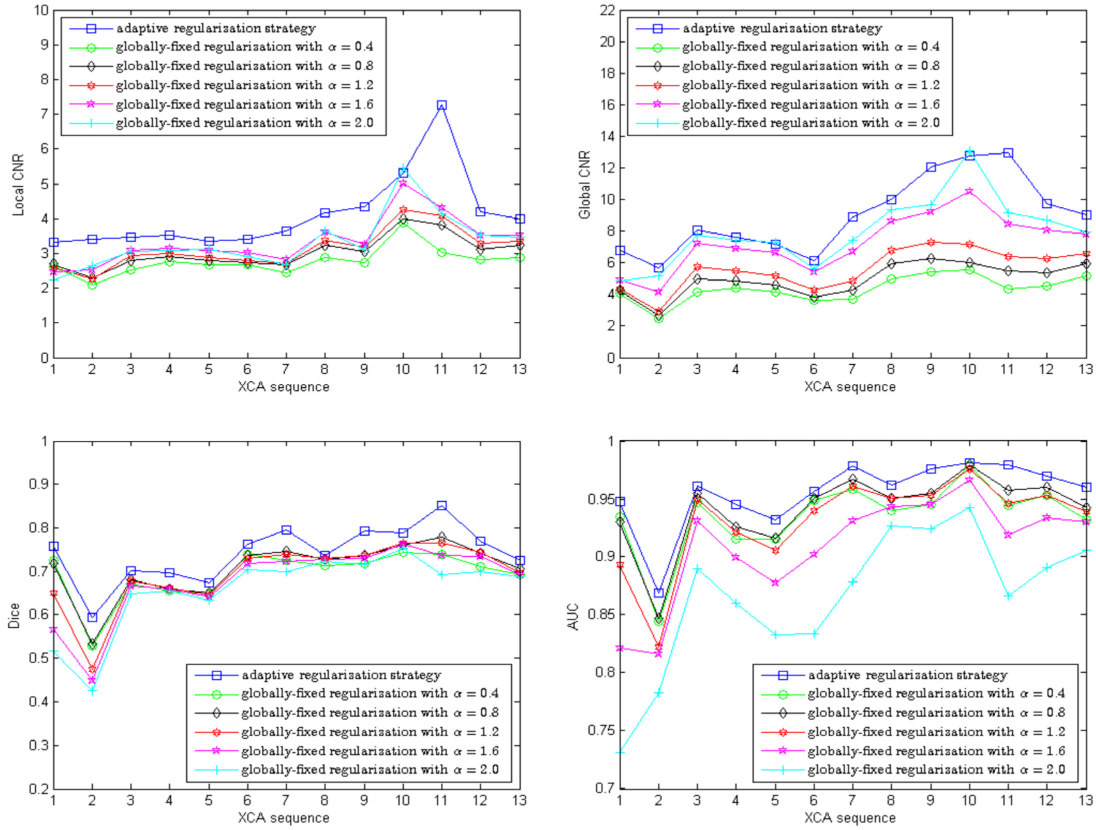

Figure 7. A comparison between the adaptive regularization and globally-fixed regularization with different values of α: the upper left and upper right figures show the local CNR and global CNR; the bottom left and bottom right figures show the Dice and AUC values, respectively.

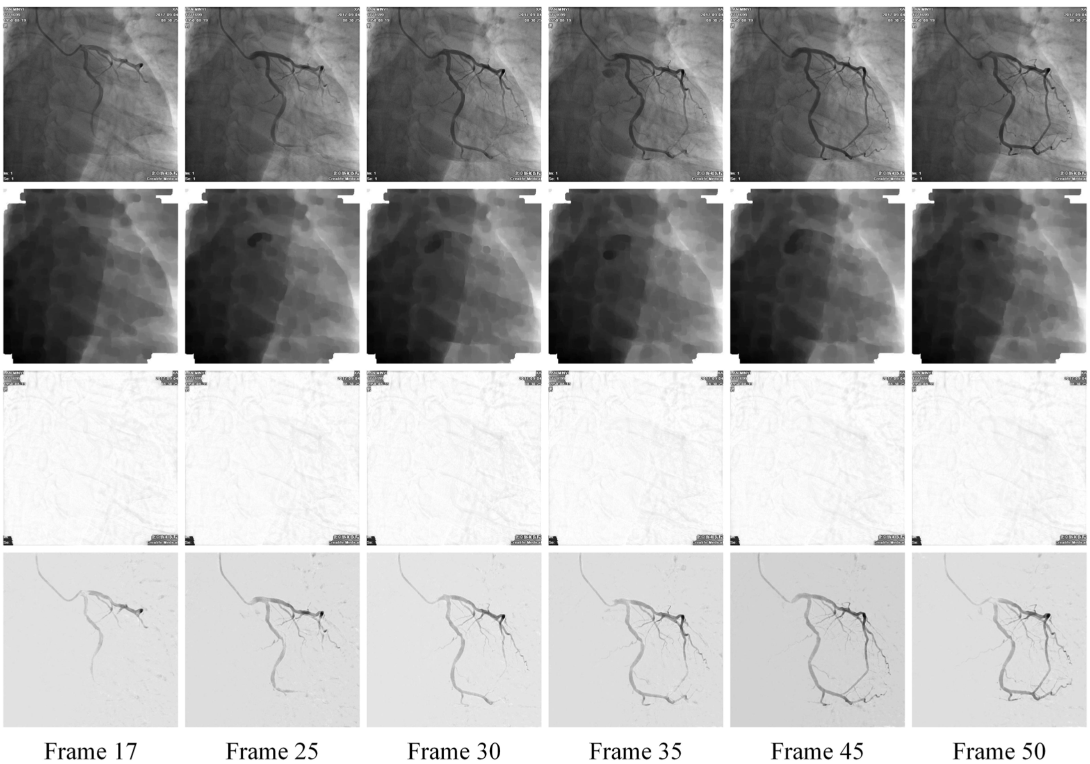

Figure 8. The layer separation results of an XCA sequence using VC-RPCA with the optimal parameters: rows 1–4 show the original XCA frames, the large-scale structure layers, the background layers and the vessel layers. Columns 1–6 are images at the 17th, 25th, 30th, 35th, 40th, 45th and 50th frame, respectively.

Figure 6 shows the sensitivity of the results to different values of parameters. First, α controls the sparsity of the foreground in the low-rank decomposition framework. Its optimal value was suggested by Candès *et al* (2011) to be exhaustively explored for specific application, i.e. the vessel enhancement. Figure 6(a) shows the performance with different values of α (here θ_L and θ_U were fixed to 0.01 and 0.15 respectively). This demonstrates that a maximal AUC can be achieved when α is in the range of $[0.4,\ 1.8]$. Therefore, the optimal α value was selected as 1.6 for adaptive regularization in the low-rank decomposition framework. Second, we performed a histogram stretch with parameters θ_L and θ_U to highlight the vesselness response of vessel-like structures. Figure 6(b) shows the effect of θ_L and θ_U on the enhancement performance with $\alpha = 1.6$. According to figure 6(b), we found that the performance is more sensitive to θ_U than θ_L. The optimal histogram stretch parameters are set as $\theta_L = 0.01$ and $\theta_U = 0.15$ to generate the vessel-like appearance prior.

Figure 7 shows a comparison between an adaptive and globally fixed regularization strategy for VC-RPCA. We tested the latter with different values of α that are globally fixed. The result shows that the adaptive regularization strategy outperforms the globally fixed strategy for all the tested sequences. The higher local and global CNRs achieved by the adaptive regularization strategy indicate that it leads to better vessel visibility, and its higher Dice coefficient and AUC show that it has fewer false positives and false negatives. Figure 8 presents the layer separation results of six selected frames from a complete angiogram sequence, and they were obtained by VC-RPCA with the optimal parameters. At the 17th frame, the contrast agent was injected into vessels through the inserted catheter tip. Vessel bifurcations in the distal end cannot be observed, since the contrast agent had not yet been distributed there. At the 25th, 30th, 35th, 40th and 45th frames, the contrast agent gradually spread for visualization of the entire vessel tree. Finally, at the 50th frame, the contrast agent started fading and the vessels near the catheter tip were blurry. The coronary tree was sufficiently maintained in the separated vessel layers of all six frames. At the same time, complex background structures were almost absorbed in the large-scale structure layers and background layers.

3.4. Experiment 2: robustness to false positives of the vessel-like appearance prior

To solve the scale issue and extract vessels with attenuate motion, the proposed VC-RPCA method extends the classical sparse and low-rank decomposition by incorporating a customized vessel-like appearance prior. The vessel-like appearance prior captures the curvilinear nature of vessels based on the Frangi filter. However, it inevitably contains false positives for curvilinear background structures, such as the edges of the pericardium, the diaphragm, the electrocardiogram monitor wire, the ribs, the sternum and the vertebra bodies, etc. An investigation of whether VC-RPCA is misguided by false positives in the vessel-like appearance prior is therefore performed.

Figure 9 shows the layer separation results on three selected frames. Each of them contain curvilinear background structures that introduce false positives to the vessel-like appearance prior. For the pericardium, the ribs and the electrocardiogram monitor wire in the first example, their strong false positives cannot be straightforwardly distinguished from vessels merely based on the vessel-like appearance prior. Even worse, these structures overlap with the target vessels due to the 2D x-ray projection operation. Similarly, the ribs, sternum, vertebra bodies and diaphragm border cause noticeable false positives in the second and third cases. After the morphological closing operation, the pericardium contour and the diaphragm border were captured by the large-scale structure layer, and did not leave artifacts in the final separated vessel layer. After the low-rank decomposition, the electrocardiogram monitor wire, ribs, sternum and vertebra bodies were absorbed in the background layer, leading to a clean vessel layer. The proposed VC-RPCA shows high robustness to the false positives of the vessel-like appearance prior, benefitting from the morphological pre-processing step and the spatio-temporal property considered in the low-rank decomposition.

3.5. Experiment 3: comparison with other RPCA methods

To further illustrate the superiority of the vessel-like appearance prior, the VC-RPCA is compared to other state-of-the-art RPCA methods that use other types of foreground priors: PCP (Ma *et al* 2015) with a naïve-sparsity-constraint-based foreground prior, PRMF (Wang *et al* 2012) with a Laplace-error-model-based foreground prior, MRC-RPCA (Jin *et al* 2017) with a motion-constraint-based foreground prior, and DECOLOR (Zhou *et al* 2013) and TFOCS (Becker *et al* 2011) with a smoothness- constraint-based foreground prior. We downloaded the source codes of these methods from the authors' homepages and optimized their parameters for our vessel enhancement task: PCP[4] adopted $\lambda = 0.8/\sqrt{\max(m, T)}$ and the convex optimization parameter setting $\mu_0 = 1.25/\|D\|^2$, $\rho = 1.5$, $J(D) = \max(\|D\|_2, \lambda^{-1}\|D\|_\infty)$; PRMF[5] set $r_k = 1$, $\lambda_u = \lambda_v = 1.5$; MRC-RPCA[6] controlled the outliers in the MoG-RPCA step with $K = 5$; DECOLOR[7] took advantage of the SOFT-IMPUTE

[4] https://github.com/dfm/pcp
[5] http://winsty.net/prmf.html
[6] http://www4.comp.polyu.edu.hk/~cslzhang/code/MoG-RPCA.rar
[7] https://fling.seas.upenn.edu/xiaowz/dynamic/wordpress/decolo

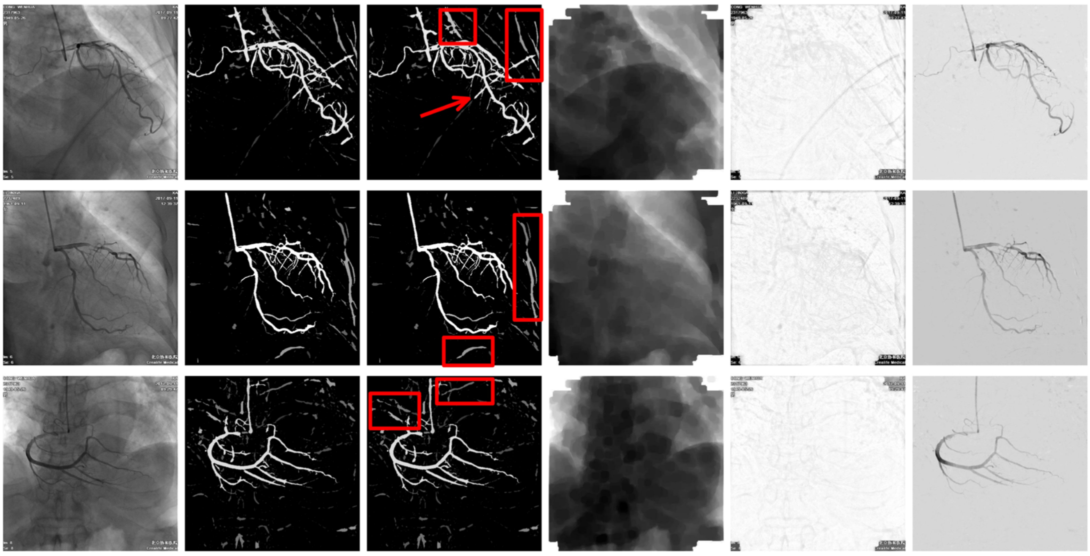

Figure 9. Examples for verifying the robustness to false positives in the vessel-like appearance prior: rows 1–3 are angiograms selected from three different XCA sequences. Columns 1–6 show the original XCA, the vessel-like appearance prior, the highlighted false positive, the large-scale structure layer, the background layer and the vessel layer.

Table 1. The performance (mean $\pm$ standard deviation) and computation time of different methods over all XCA sequences. The best performance is highlighted in bold.

Method	Dice	AUC	Local CNR	Global CNR	Computation time (s)
VC-RPCA	**0.742 $\pm$ 0.065**	**0.955 $\pm$ 0.030**	**4.106 $\pm$ 1.103**	**8.999 $\pm$ 2.423**	102.573
PCP	0.706 $\pm$ 0.064	0.941 $\pm$ 0.033	3.226 $\pm$ 0.471	5.965 $\pm$ 1.032	65.411
PRMF	0.714 $\pm$ 0.061	0.952 $\pm$ 0.027	3.157 $\pm$ 0.512	5.067 $\pm$ 1.041	197.351
MRC-RPCA	0.726 $\pm$ 0.060	[a]0.951 $\pm$ 0.032	3.562 $\pm$ 0.736	6.911 $\pm$ 1.432	1923.247
DECOLOR	0.716 $\pm$ 0.088	0.945 $\pm$ 0.042	3.711 $\pm$ 0.934	7.260 $\pm$ 2.032	186.604
TFOCS	0.697 $\pm$ 0.062	0.938 $\pm$ 0.030	2.842 $\pm$ 0.349	4.226 $\pm$ 0.810	233.222
Original XCA	0.235 $\pm$ 0.121	0.748 $\pm$ 0.087	1.192 $\pm$ 0.396	0.747 $\pm$ 0.238	N/A

[a] The comparable performance is based on a two-sided Wilcoxon signed-rank test at 95% significance level.

algorithm to iteratively obtain β and then let $\gamma = 2\beta$; TFOCS[8] made $\breve{\lambda} = 0.04$ for a better interface producer. Experiments were implemented in MATLAB R2014a (The MathWorks, Inc., Natick, MA, USA) installed on a computer with an Intel Core i5-6400 CPU (2.70 GHz) and 8 GB RAM.

Table 1 and figure 10 show a quantitative comparison of these methods. The highlighted values demonstrate that the proposed VC-RPCA method outperforms the other image decomposition methods with the two-sided Wilcoxon signed-rank test. The consistently higher local and global CNR of VC-RPCA revealed more sufficient vessel extraction and a better vessel visibility in the separated vessel layer. The higher Dice coefficient and AUC value (bottom right plot in figure 10) of our method further emphasized the accurate vessel enhancement with fewer false positives and false negatives. Despite the comparable AUC achieved by MRC-RPCA, our method was computationally fast and achieved prominently competitive vessel visibility, owing to there being less vessel residue in the background layer.

Figures 11 and 12 present visual comparisons of these RPCA methods for XCA sequences of the right and left coronary artery, respectively. Among the evaluated methods, VC-RPCA accurately preserved the fine coronary tree in the vessel layer, with a hardly observable residue in the background layer. All the other methods suffered from unsatisfactory foreground extraction and left blurry vessel structures in the background layer, as highlighted by red arrows. Their vessel residue in the background layer resulted in a lower vessel contrast and, further, a smaller CNR than VC-RPCA, as shown in table 1 and figure 10. Even worse, these methods falsely enhanced the background semi-transparent structures and led to noticeable background disturbance in the vessel layer, as highlighted by purple boxes. The visual comparison demonstrates the superiority of our method for its effective background suppression and accurate vessel extraction.

[8] http://cvxr.com/tfocs/download/

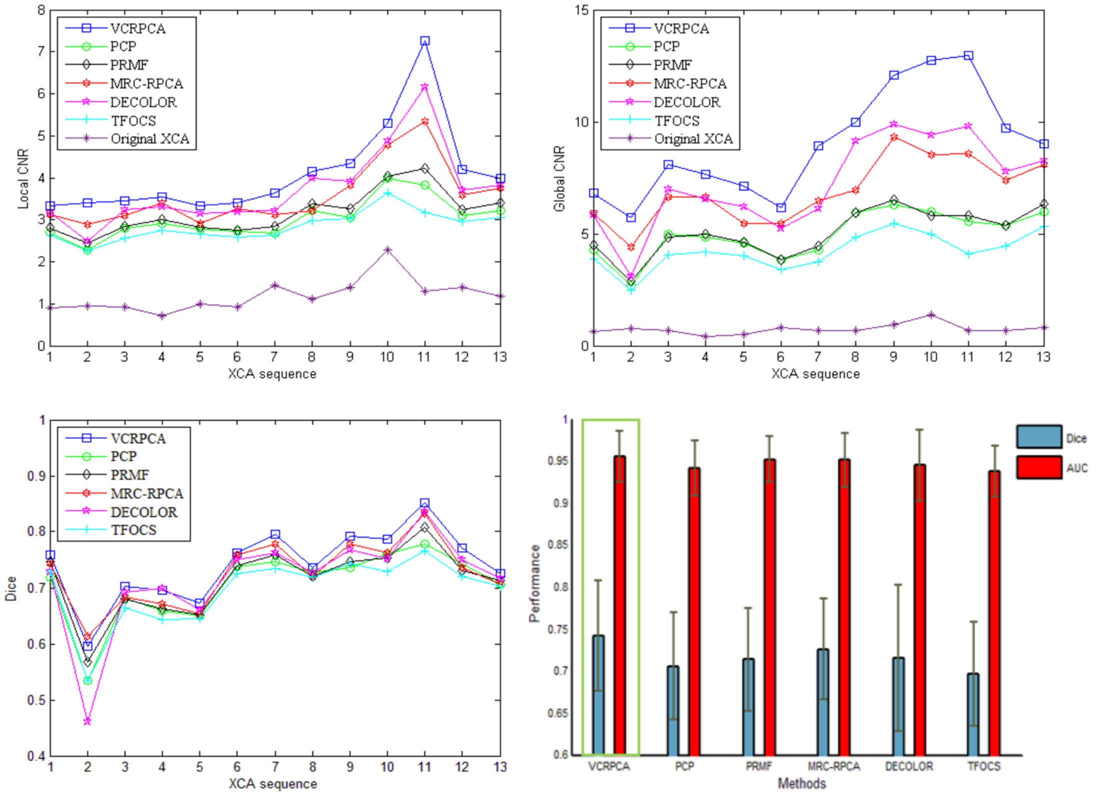

Figure 10. A quantitative comparison of different RPCA methods for all XCA sequences: local CNR (upper left), global CNR (upper right), Dice (bottom left) along with AUC statistically shown in the bottom right, where the best performance is highlighted by a green bounding box.

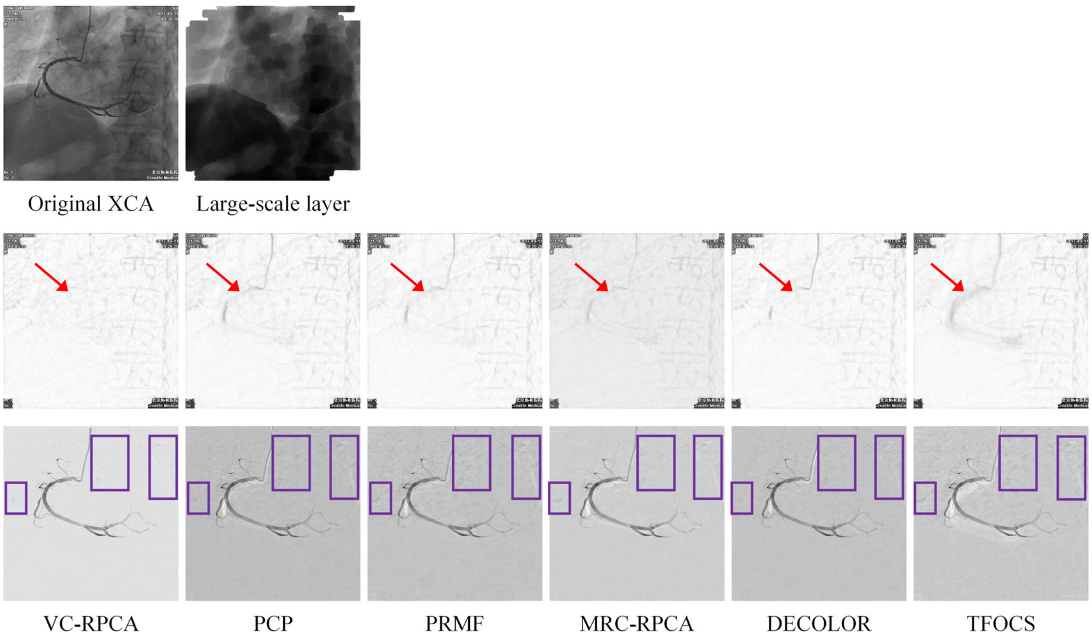

Figure 11. A visual comparison of different RPCA methods for the XCA of the right coronary artery. The first row shows the original XCA and the large-scale structure layer. The background layer and vessel layer are presented in rows 2–3, where each column is obtained by different methods. Compared with other methods, our VC-RPCA has a better ability to remove vessel residue in the background layer (highlighted by red arrows), and suppress background disturbance in the vessel layer (highlighted by purple boxes).

3.6. Experiment 4: layer separation in a low-contrast scenario

3.6.1. Preparation for synthetic low-contrast angiograms

A promising application of layer separation is to improve vessel visibility, especially under the condition of low-contrast concentration. To investigate the performance of our method in situations where the injected contrast

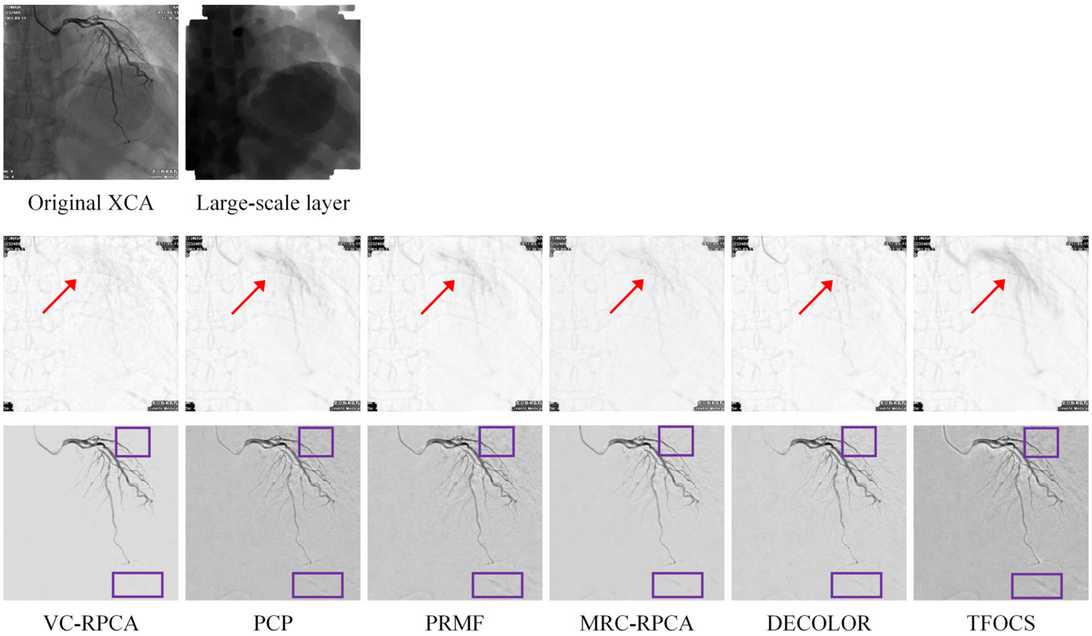

Figure 12. A visual comparison of different RPCA methods for the XCA of the left coronary artery. The first row shows the original XCA and the large-scale structure layer. The background layer and vessel layer are presented in rows 2–3, where each column is obtained by different methods. Compared with other methods, our VC-RPCA has a better ability to remove vessel residue in the background layer (highlighted by red arrows), and suppress background disturbance in the vessel layer (highlighted by purple boxes).

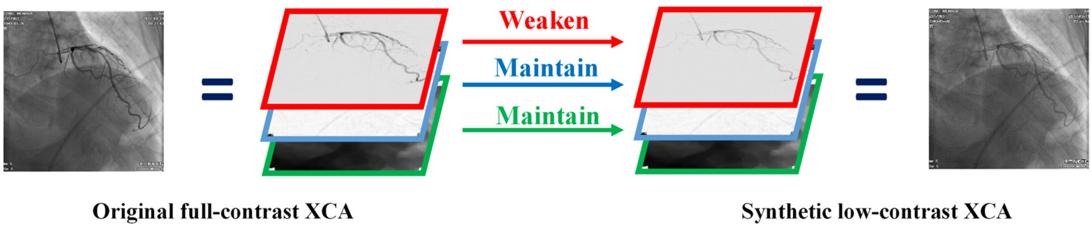

Figure 13. The synthesis of a low-contrast XCA from a layer separation perspective. The vessel layer (in the red box), the background layer (in the blue box) and the large-scale structure layer (in the green box) are separated, weakened/maintained and added back to compose a low-contrast image.

agent has a low concentration, we synthesized low-contrast angiograms from real full-contrast XCAs.

To synthesize low-contrast images, we model an x-ray angiogram as a superposition of three layers including a large-scale structure layer, a background layer and a vessel layer. In the clinical workflow, the cardiologist injects an x-ray contrast agent of low concentration and then collects low-contrast angiograms on the 2D projection plane. From the layer separation perspective, the reduced contrast agent only affects the vessel layer and has no influence on the other two layers. Therefore, motivated by Ma *et al* (2017), the synthetic low-contrast data should only be simulated by weakening the vessel layer separated from the original full-contrast image, leaving the background layer and large-scale structure layer unchanged. Figure 13 shows the synthesis of a low-contrast XCA. The original full-contrast image $\boldsymbol{I}_{\text{Full-contrast}}$ was firstly separated into a vessel layer $\boldsymbol{I}_{\text{Vessel}}$, a background layer $\boldsymbol{I}_{\text{Background}}$ and a large-scale structure layer $\boldsymbol{I}_{\text{Large-scale}}$. Then the low-contrast image $\boldsymbol{I}_{\text{Low-contrast}}$ was generated as the sum of $\boldsymbol{I}_{\text{Background}}$, $\boldsymbol{I}_{\text{Large-scale}}$ and a weakened $\boldsymbol{I}_{\text{Vessel}}$:

$$\boldsymbol{I}_{\text{Low-contrast}} = \varepsilon \boldsymbol{I}_{\text{Vessel}} + \boldsymbol{I}_{\text{Background}} + \boldsymbol{I}_{\text{Large-scale}}$$

$$\text{s.t. } \boldsymbol{I}_{\text{Full-contrast}} = \boldsymbol{I}_{\text{Vessel}} + \boldsymbol{I}_{\text{Background}} + \boldsymbol{I}_{\text{Large-scale}}, \quad (13)$$

where the factor $\varepsilon < 1$ accounts for the synthetic low-contrast concentration, which means that reducing the signal of the vessel layer leads to a lower contrast between the vessel and the background, i.e. a lower CNR.

These three separated layers are important for the simulation of low-contrast images. Unfortunately, they are gray-level images rather than binary masks. Hao *et al* (2018) pointed out that an absolutely authentic vessel layer cannot be achieved, even with manual vessel identification. In this work, we relied on the MRC-RPCA method to separate the original full-contrast XCA, and then synthesized the low-contrast image with $\varepsilon = 0.5$. This can avoid biasing the performance of vessel enhancement towards our VC-RPCA method.

Table 2. The performance (mean ± standard deviation) of different methods in the low-contrast scenario. The best performance is highlighted in bold.

Method	Dice	AUC	Local CNR	Global CNR
VC-RPCA	**0.714 ± 0.082**	**0.944 ± 0.036**	**3.534 ± 0.792**	**6.666 ± 0.036**
PCP	0.679 ± 0.068	0.932 ± 0.036	2.708 ± 0.387	4.060 ± 0.830
PRMF	0.689 ± 0.064	[a]0.944 ± 0.029	2.843 ± 0.422	4.162 ± 0.842
MRC-RPCA	[a]0.700 ± 0.066	[a]0.934 ± 0.037	3.123 ± 0.672	5.753 ± 1.305
DECOLOR	0.658 ± 0.087	0.922 ± 0.043	2.827 ± 0.645	4.420 ± 1.376
TFOCS	0.697 ± 0.063	0.932 ± 0.031	2.842 ± 0.349	4.226 ± 0.810
Synthetic low-contrast XCA	0.156 ± 0.089	0.675 ± 0.093	0.867 ± 0.282	0.527 ± 0.219
Original full-contrast XCA	0.235 ± 0.121	0.748 ± 0.087	1.192 ± 0.396	0.747 ± 0.238

[a] The comparable performance is based on a two-sided Wilcoxon signed-rank test at 95% significance level.

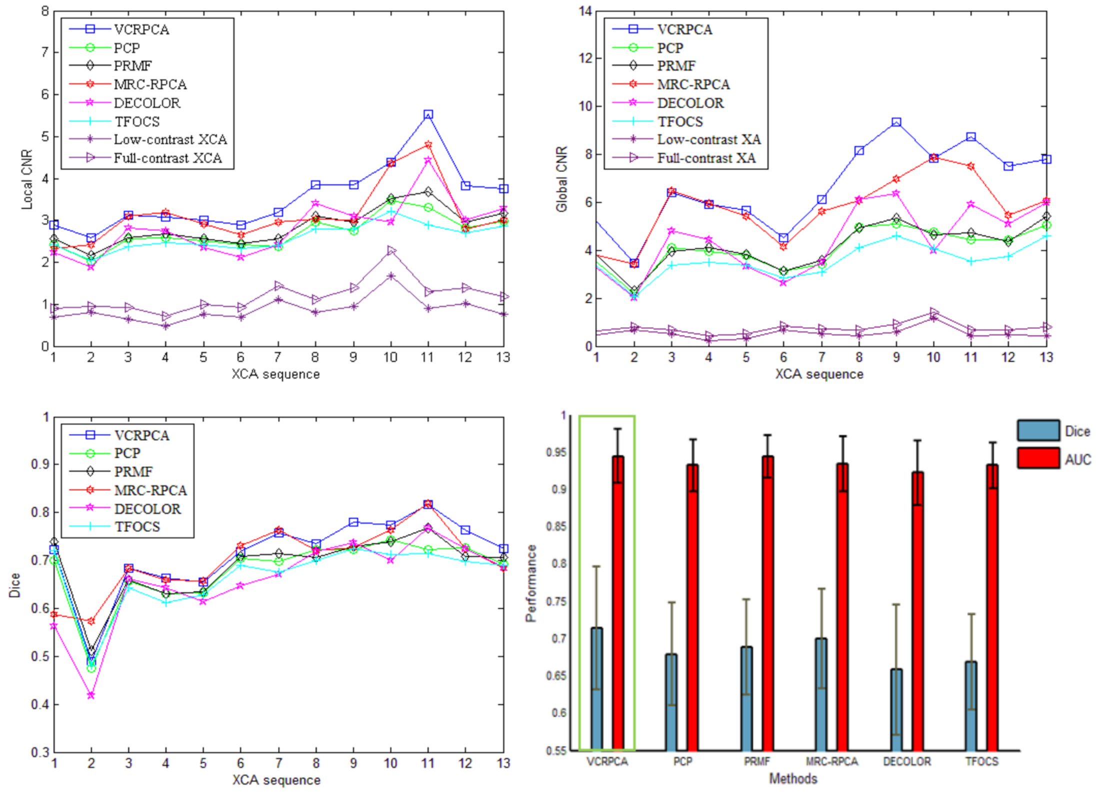

Figure 14. A quantitative comparison of different RPCA methods in the low-contrast scenario: local CNR (upper left), global CNR (upper right) and Dice (bottom left), along with the AUC statistically shown in the bottom right, where the best performance is highlighted by a green bounding box.

3.6.2. Layer separation for synthetic low-contrast angiograms

We used different RPCA methods to improve the poor vessel visibility in synthetic low-contrast sequences. Quantitative comparisons between these methods are illustrated in table 2 and figure 14. The proposed VC-RPCA method achieved not only the highest CNR but also the highest Dice coefficient and AUC. MRC-RPCA and PRMF obtained a comparable Dice coefficient and AUC to VC-RPCA, while achieving a lower vessel contrast in the enhancement results.

Figures 15 and 16 show the layer separation results obtained by different RPCA methods for synthetic low-contrast XCA sequences of the right and left coronary artery, respectively. The low-contrast concentration led to a coarse vessel-like appearance prior, where some continuous vessels are broken and missed (highlighted by green circles). The VC-RPCA was not misguided by these false negatives, and it successfully captured the complete and continuous coronary tree with the best background suppression in the vessel layer (highlighted by purple boxes). Among the evaluated methods, VC-RPCA also had the least vessel residue in the background layer (highlighted by red arrows), which at the same time improved vessel visibility. Compared with experiment 3 in the full-contrast situation, all the other methods had slightly better vessel extraction and left less

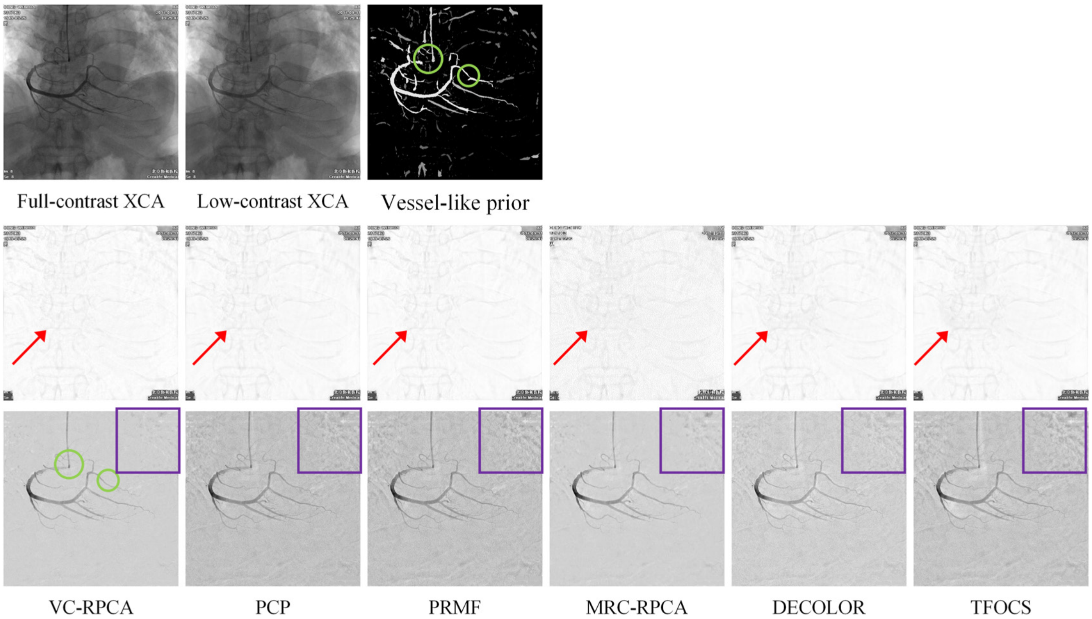

Figure 15. A visual comparison of different RPCA methods for the synthetic low-contrast XCA of the right coronary artery: the first row shows the original full-contrast XCA, the simulated low-contrast XCA and the vessel-like prior under this low-contrast condition. The background layer and the vessel layer are presented in rows 2–3, where each column corresponds to different methods. Our VC-RPCA shows robustness to false negatives in the vessel-like appearance prior, i.e. the broken and missed branches (highlighted by green circles). Compared with other methods, our VC-RPCA also has a better ability to remove vessel residue from the background layer (highlighted by red arrows), and suppress background disturbance in the vessel layer (highlighted by purple boxes).

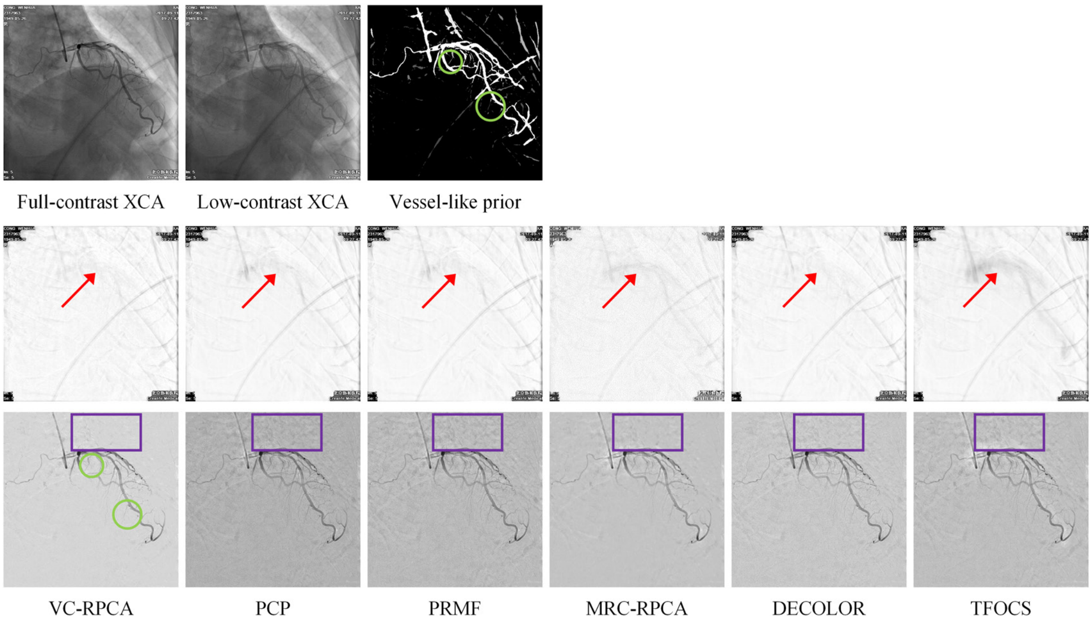

Figure 16. A visual comparison of different RPCA methods for the synthetic low-contrast XCA of the left coronary artery: the first row shows the original full-contrast XCA, the simulated low-contrast XCA and the vessel-like prior under this low-contrast condition. The background layer and the vessel layer are presented in rows 2–3, where each column corresponds to different methods. Our VC-RPCA shows robustness to false negatives in the vessel-like appearance prior, i.e. the broken and missed branches (highlighted by green circles). Compared with other methods, our VC-RPCA also has a better ability to remove vessel residue from the background layer (highlighted by red arrows), and suppress background disturbance in the vessel layer (highlighted by purple boxes).

vessel residue in the background layer. However, they suffered from more background disturbance and were not able to ensure a substantially clean vessel layer. Based on this experiment, we found that the proposed VC-RPCA method outperformed all the counterpart methods with the best vessel visibility as well as the lowest false positive/negative rate.

4. Discussion and conclusions

Vessel enhancement for coronary arteries in x-ray angiograms is critical for the accurate diagnosis of coronary artery disease and pre-intervention decision-making. To separate vessels with attenuate motion from overlapped complex background structures, we proposed a structured-sparse, low-rank decomposition framework called vessel-constrained RPCA, which utilizes a novel vessel-like appearance prior. For vessel enhancement, the proposed VC-RPCA method separates an angiogram into three layers: a large-scale structure layer, a background layer and a vessel layer that contains coronary arteries. This relies on the morphological closing operation, the vessel-like appearance prior and the VC-RPCA decomposition, where the regularization parameter is adaptively adjusted to ensure an accurate enhancement of vessels with various sizes and attenuate motion. Qualitative and quantitative evaluations show the superiority of VC-RPCA for vessel enhancement in the clinical x-ray angiogram.

Unlike any other existing foreground priors in RPCA methods, the proposed vessel-like prior exploits curvilinear appearance features and provides a structured-sparse constraint that is robust to the motion variation of vessels in angiogram sequences. To illustrate the superiority of the proposed vessel-like appearance prior, experiment 3 compares the VC-RPCA method with various state-of-the-art RPCA methods that utilize other foreground priors. With a naïve-sparsity-constraint-based foreground prior, PCP cannot distinguish vessels with attenuate motion from the low-rank background layer. Therefore, this tends to leave evident the ghostly presence of vessel residue in the background layer. With the Laplace error model-based foreground prior, PRMF has a high detection rate for moving vessels but simultaneously enhances the moving semi-transparent background structures. With the motion constraint-based foreground prior, MRC-RPCA focuses on the spatio-temporal contiguity of foreground trajectories in a graduated RPCA scheme. The used total variation regularization lacks discrimination for vessels with attenuate motion, leading to insufficient vessel extraction and, further, worse vessel enhancement performance. With the smoothness-constraint-based foreground prior, DECOLOR is affected by contiguous background disturbance, since the coarse Markov prior is usually confused by the spatially coherent clusters. Also, the perennial over-smoothness and shortcutting phenomenon (Kolmogorov and Boykov 2005) degrades the vessel enhancement performance. TFOCS achieves the worst performance due to its oversimplified smoothness constraint based on templates for convex cone problems. With the novel vessel-like appearance prior based on curvilinear features, the proposed VC-RPCA method accurately captures contrast-filled vessels in the clean vessel layer and leaves no vessel residue in the background layer. This can prominently improve vessel visibility without incurring a large false positive/negative rate.

The adaptive regularization strategy contributes to solving the scale issue in the vessel enhancement task, where the low-rank decomposition is challenged by the various sizes of the vessels. A single globally fixed regularization parameter λ cannot ensure the effective detection of vessels of all sizes. Specifically, a globally small λ for motion compensation usually causes false-positive extraction, while a globally-large λ cannot achieve adequate vessel detection in the vessel layer. To solve the scale issue, we specifically adopt a small λ for vessel-like regions that is constrained by structured sparsity, making the algorithm sensitive to vessels even with attenuate motion. At the same time, we use a large λ for background regions to suppress background disturbance in the vessel layer. Experiment 1 demonstrates that the proposed adaptive regularization strategy has an obvious advantage over the non-adaptive strategy used in the same decomposition framework. The separated vessel layer can capture thin branches with small scales without introducing background disturbance.

In addition, the proposed VC-RPCA method is robust against false positives and false negatives in the vessel-like appearance prior. False positives are related to the curvilinear features that cannot distinguish between vessels and curvilinear background structures, such as the diaphragm border, pericardium contour, sternum, ribs and vertebral body edges, etc. The proposed VC-RPCA adopts a list of operations to eliminate these false-positive background structures. Firstly, a diaphragm border and pericardium contour are distinguishable due to their relatively large scales. They can be extracted from the large-scale structure layer via a morphological closing operation, avoiding strong artifacts in the output vessel layer. Secondly, the remaining false-positive background structures usually have quasi-static motion, which is modeled by the nuclear norm in the VC-RPCA decomposition framework. The beneficial temporal property, neglected by the vessel-like appearance prior, facilitates the absorption of these background structures into the low-rank background layer. In experiment 2, despite noticeable false positives in the vessel-like appearance prior, there is almost no background disturbance in the separated vessel layer. False negatives arise from the poor contrast and faint intensity edge in the XCA, leading to broken and missed vessels in the vessel-like appearance prior. This issue is severer in the low-contrast scenario, as shown in experiment 4. The coarse appearance cue is refined and compensated by the motion cue, which is modeled by a low-rank pattern in the decomposition framework. Therefore, the continuity and completeness of vessels can be ensured even with false negatives in the vessel-like appearance prior.

The performance shown in experiment 4 also implies the potential application of VC-RPCA in improving the diagnosis quality with a reduced contrast agent. In this work, we synthesized low-contrast data from a weakened vessel layer instead of a manual identified vessel mask. If we use a binary vessel mask and directly weaken the vessel region in the original full-contrast image, it will inevitably change the same vessel region in the background and the large-scale structure layers at the same time, and is unable to ensure a change in the vessel layer only. This operation violates the physiological process of low-contrast concentration, making it unable to synthesize a reasonable low-contrast image. Experimental results show that in the low-contrast scenario, poorer vessel visibility further degrades the low-rank decomposition and hampers the accurate separation of vessels with attenuate motion. All other state-of-the-art methods suffer from more background disturbance compared with experiment 3 in the full-contrast situation. Their foreground priors seem over-loose and fuzzy between the background and low-contrast vessels. Therefore, they cannot maintain a reasonable balance between vessel extraction and background suppression. In contrast, our VC-RPCA method can achieve a simultaneously satisfactory vessel and background layers after the low-rank decomposition. The proposed vessel-like appearance prior shows a great advantage over the other existing foreground priors, and enables the superior performance of vessel enhancement under low-contrast conditions.

During coronary angiography, the cardiologist inserts the catheter through the coronary sinus and injects a contrast agent through it to visualize the target coronary vessels. The catheter tip can always be observed in each frame of the XCA sequence. However, it is still intractable for layer separation methods to accurately exclude this structure in the vessel layer (Ma *et al* 2015, 2017, Jin *et al* 2017). In future work, it would be of interest to investigate a discriminative model and develop an advanced appearance feature that can distinguish the catheter tip and vessels. Improved by this prior, VC-RPCA can further facilitate more accurate vessel enhancement, without being confused by the catheter tip.

Our future study will also focus on developing a multi-prior strategy in the proposed decomposition framework, to leverage the strengths of all used priors. Owing to the vessel-like appearance prior, the proposed VC-RPCA can well detect most vessel branches, even under conditions of low concentration. However, a small fraction of tiny vessels is still missed due to their faint intensity edge and simultaneously non-salient motion pattern. We believe that this phenomenon can be relieved by integrating more foreground priors (e.g. motion coherence and smoothness constraint) rather than merely using an appearance prior. These priors would appropriately relax the foreground constraint on vessel-like regions, contributing to the preservation of more tiny branches in the vessel layer. This unified multi-prior strategy is expected to be a promising solution to the refined enhancement of the tiny branches in XCA sequences.

In conclusion, we have proposed a novel layer separation framework for vessel enhancement in XCAs, using a structured-sparse, low-rank decomposition called vesselness-constrained RPCA. Benefiting from the novel vessel-like appearance prior, the proposed method outperforms existing state-of-the-art RPCA methods, and significantly improves vessel visibility without intolerable computational complexity— even in the low-contrast scenario.

Acknowledgments

The authors gratefully acknowledge Premal Patel for his help in proofreading this paper. This research is partially supported by the National Key research and development program (2016YFC0106200), the 863-national research fund (2015AA043203), the Chinese NSFC research fund (61190120, 61190124 and 61271318) and the special funding of capital health research and development with No. 2016-1-4011.

ORCID iDs

Lixu Gu https://orcid.org/0000-0002-6210-4847

References

Andreucci M, Solomon R and Tasanarong A 2014 Side effects of radiographic contrast media: pathogenesis, risk factors, and prevention *Biomed. Res. Int.* **2014** 20

Baka N, Lelieveldt B, Schultz C, Niessen W and van Walsum T 2015 Respiratory motion estimation in x-ray angiography for improved guidance during coronary interventions *Phys. Med. Biol.* **60** 3617

Baka N, Metz C, Schultz C, Neefjes L, van Geuns R J, Lelieveldt B P, Niessen W J, van Walsum T and de Bruijne M 2013 Statistical coronary motion models for 2D+ t/3D registration of x-ray coronary angiography and CTA *Med. Image Anal.* **17** 698–709

Becker S R, Candès E J and Grant M C 2011 Templates for convex cone problems with applications to sparse signal recovery *Math. Prog. Comput.* **3** 165

Bouwmans T, Sobral A, Javed S, Jung S K and Zahzah E-H 2017 Decomposition into low-rank plus additive matrices for background/foreground separation: a review for a comparative evaluation with a large-scale dataset *Comput. Sci. Rev.* **23** 1–71

Candès E J, Li X, Ma Y and Wright J 2011 Robust principal component analysis? *J. ACM* **58** 1–37

Chen M, Ganesh A, Lin Z, Ma Y, Wright J and Wu L 2009 Fast convex optimization algorithms for exact recovery of a corrupted low-rank matrix *Coordinated Science Laboratory Report no.* UILU-ENG-09-2214

Çimen S, Gooya A, Grass M and Frangi A F 2016 Reconstruction of coronary arteries from x-ray angiography: a review *Med. Image anal.* **32** 46–68

Dodge J T, Brown B G, Bolson E L and Dodge H T 1992 Lumen diameter of normal human coronary arteries. Influence of age, sex, anatomic variation, and left ventricular hypertrophy or dilation *Circulation* **86** 232–46

Dumay A C, Reiber J H and Gerbrands J J 1994 Determination of optimal angiographic viewing angles: basic principles and evaluation study *IEEE Trans. Med. Imaging* **13** 13–24

Fischer P, Pohl T, Köhler T, Maier A and Hornegger J 2015 A robust probabilistic model for motion layer separation in x-ray fluoroscopy *Int. Conf. on Information Processing in Medical Imaging* (Berlin: Springer) pp 288–99

Frangi A F, Niessen W J, Vincken K L and Viergever M A 1998 Multiscale vessel enhancement filtering *Int. Conf. on Medical Image Computing and Computer-Assisted Intervention* (Berlin: Springer) pp 130–7

Gao Z, Cheong L-F and Wang Y-X 2014 Block-sparse RPCA for salient motion detection *IEEE Trans. Pattern Anal.* **36** 1975–87

Hao H, Ma H and van Walsum T 2018 Vessel layer separation in x-ray angiograms with fully convolutional network *Medical Imaging 2018: Image-Guided Procedures, Robotic Interventions, and Modeling* (International Society for Optics and Photonics) p 105761V

Hyvärinen A and Oja E 2000 Independent component analysis: algorithms and applications *Neural Netw.* **13** 411–30

Jin M, Li R, Jiang J and Qin B 2017 Extracting contrast-filled vessels in x-ray angiography by graduated RPCA with motion coherency constraint *Pattern Recogn.* **63** 653–66

Kolmogorov V and Boykov Y 2005 What metrics can be approximated by geo-cuts, or global optimization of length/area and flux *10th IEEE Int. Conf. on Computer Vision, 2005 (ICCV 2005)* (IEEE) pp 564–71

Lesage D, Angelini E D, Bloch I and Funka-Lea G 2009 A review of 3D vessel lumen segmentation techniques: models, features and extraction schemes *Med. Image Anal.* **13** 819–45

Lin Z and Wei S 2010 A block Lanczos with warm start technique for accelerating nuclear norm minimization algorithms (arXiv:1012.0365)

Lin Z, Chen M and Ma Y 2010 The augmented Lagrange multiplier method for exact recovery of corrupted low-rank matrices (arXiv:1009.5055)

Ma H, Dibildox G, Banerjee J, Niessen W, Schultz C, Regar E and van Walsum T 2015 Layer separation for vessel enhancement in interventional x-ray angiograms using morphological filtering and robust PCA *Workshop on Augmented Environments for Computer-Assisted Interventions* (Berlin: Springer) pp 104–13

Ma H, Hoogendoorn A, Regar E, Niessen W J and van Walsum T 2017 Automatic online layer separation for vessel enhancement in x-ray angiograms for percutaneous coronary interventions *Med. Image Anal.* **39** 145–61

Merveille O, Talbot H, Najman L and Passat N 2018 Curvilinear structure analysis by ranking the orientation responses of path operators *IEEE Trans. Pattern Anal.* **40** 304–17

Panayiotou M, King A P, Housden R J, Ma Y, Cooklin M, O'Neill M, Gill J, Rinaldi C A and Rhode K S 2014 A statistical method for retrospective cardiac and respiratory motion gating of interventional cardiac x-ray images *Med. Phys.* **41** 071901

Perry R, Joseph M X, Chew D P, Aylward P E and De Pasquale C G 2013 Coronary artery wall thickness of the left anterior descending artery using high resolution transthoracic echocardiography-normal range of values *Echocardiography* **30** 759–64

Rodriguez P and Wohlberg B 2013 Fast principal component pursuit via alternating minimization *2013 20th IEEE Int. Conf. on Image Processing (ICIP)* (IEEE) pp 69–73

Tang G and Nehorai A 2011 Robust principal component analysis based on low-rank and block-sparse matrix decomposition *2011 45th Annual Conf. on Information Sciences and Systems (CISS)* (IEEE) pp 1–5

Tang S, Wang Y and Chen Y-W 2012 Application of ICA to x-ray coronary digital subtraction angiography *Neurocomputing* **79** 168–72

Timinger H, Krueger S, Dietmayer K and Borgert J 2005 Motion compensated coronary interventional navigation by means of diaphragm tracking and elastic motion models *Phys. Med. Biol.* **50** 491

Ungi T, Zimmermann Z, Balázs E, Lassó A, Ungi I, Forster T, Palkó A and Nemes A 2009 Vessel masking improves densitometric myocardial perfusion assessment *Int. J. Cardiovascular Imaging* **25** 229–36

Volpi D, Sarhan M H, Ghotbi R, Navab N, Mateus D and Demirci S 2015 Online tracking of interventional devices for endovascular aortic repair *Int. J. Comput. Assist. Radiol. Surg.* **10** 773–81

Vos T, Allen C, Arora M, Barber R M, Bhutta Z A, Brown A, Carter A, Casey D C, Charlson F J and Chen A Z 2016 Global, regional, and national incidence, prevalence, and years lived with disability for 310 diseases and injuries, 1990–2015: a systematic analysis for the Global Burden of Disease Study 2015 *Lancet* **388** 1545–602

Wang H, Naghavi M, Allen C, Barber R, Carter A, Casey D, Charlson F, Chen A, Coates M and Coggeshall M 2016 Global, regional, and national life expectancy, all-cause mortality, and cause-specific mortality for 249 causes of death, 1980–2015: a systematic analysis for the Global Burden of Disease Study 2015 *Lancet* **388** 1459–544

Wang N, Yao T, Wang J and Yeung D-Y 2012 A probabilistic approach to robust matrix factorization *European Conf. on Computer Vision* (Springer) pp 126–39

Zhang W, Ling H, Prummer S, Zhou K S, Ostermeier M and Comaniciu D 2009 Coronary tree extraction using motion layer separation *Int. Conf. on Medical Image Computing and Computer-Assisted Intervention* (Berlin: Springer) pp 116–23

Zhou X, Yang C and Yu W 2013 Moving object detection by detecting contiguous outliers in the low-rank representation *IEEE Trans. Pattern Anal.* **35** 597–610

Zhu Y, Prummer S, Wang P, Chen T, Comaniciu D and Ostermeier M 2009 Dynamic layer separation for coronary DSA and enhancement in fluoroscopic sequences *Int. Conf. on Medical Image Computing and Computer-Assisted Intervention* (Berlin: Springer) pp 877–84